Robotics and Computer–Integrated Manufacturing 97 (2026) 103059

Contents lists available at ScienceDirect

Robotics and Computer-Integrated Manufacturing

journal homepage: www.elsevier.com/locate/rcim

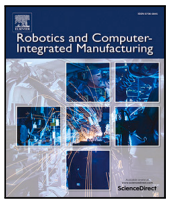

Full length article

Novel calibration method for robotic bottom-up vat polymerization additive manufacturing systems

Evan Rolland [a], Yasser Krim [a], Ahmed Joubair [a], Ilian A. Bonev [a,*], Evan Jones [b], Pengpeng Zhang [b], Cheng Sun [b], Nanzhu Zhao [c]

[a] École de technologie supérieure, 1100, Notre-Dame Street West, Montreal, H3C 1K3, QC, Canada
[b] Department of Mechanical Engineering, Northwestern University, Evanston, 60208, IL, USA
[c] Nissan Technical Center North America, 39001 Sunrise Dr., Farmington Hills, 48331, MI, USA

ARTICLE INFO

Keywords:
Robot calibration
Accuracy
Precision
Self calibration
Closed-loop calibration

ABSTRACT

This article presents a new affordable calibration method for a 7-axis robotic system used for vat polymerization 3D printing. The method employs three metrology elements: a calibration robot end-effector with three precision balls, a measurement probe composed of three linear gauges, and, notably, a kinematic coupling allowing the precise positioning of the probe onto the resin tank in three locations. The robotic system comprises a Mecademic Meca500 6-axis industrial robot mounted on a Zaber X-LRQ300AP linear guide. The calibration method consists of automatically aligning the centers of each of the three precision balls with the probe origin. This alignment is performed with different robot joint angles and linear guide displacements, and for all three locations of the probe. After calibration, the relative accuracy of the 7-axis robotic system with respect to the resin tank, as validated using a laser tracker, is improved from 1.272 mm to 0.271 mm, which is comparable to what can be achieved with significantly more expensive metrology equipment.

1. Introduction

Industrial robots are playing an increasingly important role in additive manufacturing, offering substantial advantages in terms of flexibility, scalability, and efficiency. A six-axis industrial robot arm, in particular, enables the production of complex, curved geometries that are challenging or unattainable with conventional 3D printers [1,2]. Printing with six degrees of freedom also reduces the stair-stepping effect, resulting in smoother surfaces and higher-quality prints. Additionally, robots can not only print parts but also handle them for further processing and storage, thanks to the use of tool changers.

In particular, we have recently developed an innovative 3D printing system that integrates a high-precision, 6-axis robot arm with a bottom-up projection vat polymerization system [3]. This approach offers substantial advantages over traditional 3D printing, which relies on rectilinear Z-axis motion, by enabling full degrees-of-freedom (DOF) transformations — translation, rotation, and scaling — of each individual layer, creating 3D structures through the continuous curvilinear motion of the robot arm. This approach dynamically transforms individual building layers on-the-fly, eliminating time-consuming recoating steps inherent to conventional sequential manufacturing processes, thereby enhancing surface smoothness and material homogeneity. By localizing transformations to each layer, our method achieves discrete conformal transformations, allowing for the customized fabrication of complex structures, such as vascular scaffolds, that precisely fit patient-specific anatomies derived from magnetic resonance imaging (MRI) data. Additionally, this layer-by-layer orientation control expands the process into multimaterial, multiaxis 3D printing, enabling the integration of functional components made from varied materials. Despite its promising potential, the production of high-quality 3D-printed parts still depends critically on the robotic arm's motion accuracy that matches with the desired voxel resolution at the micrometer scale.

Accuracy is critical in additive manufacturing, as the goal is to produce a printed part that closely matches the source CAD model. While off-the-shelf industrial robots are highly precise, with some achieving repeatability of up to 5 micrometers, their accuracy remains relatively poor. Accuracy, often confused with precision, refers to the robot's ability to move its end-effector to a specified position and orientation (pose) defined by Cartesian coordinates, such as those from the G-code. Even in the most precise robots, the error between the desired and actual positions of the end-effector can reach up to 1 mm.

Improving a robot's accuracy is known as robot calibration [4]. This process involves using metrology equipment, performing time-consuming measurements, developing a complex mathematical model

* Corresponding author.
E-mail address: ilian.bonev@etsmtl.ca (I.A. Bonev).

https://doi.org/10.1016/j.rcim.2025.103059
Received 22 November 2024; Received in revised form 6 May 2025; Accepted 12 May 2025
Available online 4 June 2025

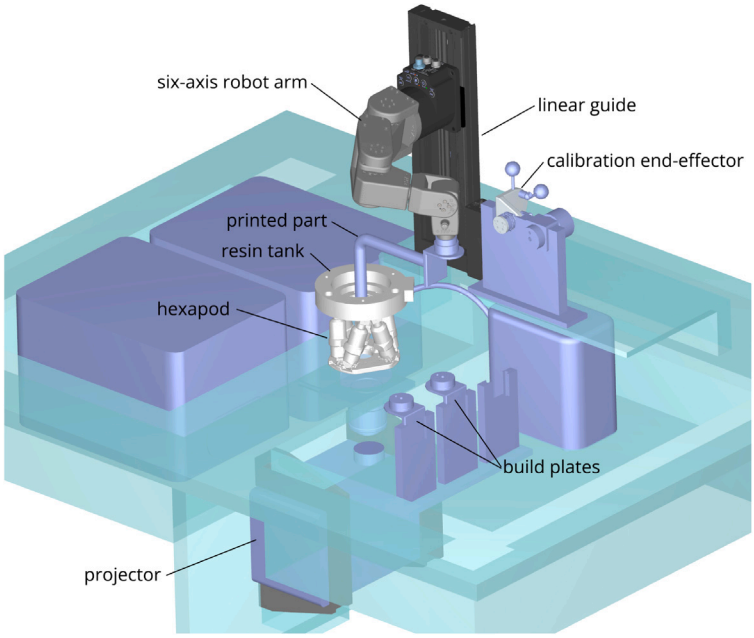

Fig. 1. Overview of the robotic projection vat polymerization additive manufacturing system under development.

of the robot, and using optimization methods to identify the parameters of that model. Many industrial robots can be purchased with factory calibration for an additional cost, typically a few thousand dollars [5]. However, this calibration only addresses one source of errors: the robot alone. The entire system must also be calibrated, including the specific end-effector, any linear guides, rotary tables, or other components in the cell. Additionally, calibration is not permanent due to wear and collisions, and periodic recalibration may be required to maintain accuracy over time. As a result, developing an on-site robot calibration procedure is often more cost-effective and, in many cases, unavoidable.

There are various methods for calibrating a robot arm or an entire robotic system, each distinguished primarily by the metrology equipment employed. The best results are typically achieved with a laser tracker [4] or a CMM (coordinate measuring machine), tools commonly used by robot manufacturers. However, a laser tracker costs more than US$80,000, while a CMM can only be used on very small robot arms (e.g., [5]). In an attempt to reduce calibration costs, methods based on the use of much more affordable metrology tools have been proposed, depending on the robotic application.

In this paper, we focus on a desktop robotic projection vat polymerization additive manufacturing system, such as the one shown in Fig. 1. The system includes a six-axis robot arm, which can be optionally mounted on a vertical linear guide. An angled build plate is attached to the robot's flange, via a tool changer. Potentially, the resin tank can be further mounted on a hexapod or another alignment device, providing additional degrees of freedom for localized manipulation of the curing interface in the additive manufacturing process. The alignment of the transparent bottom of the resin tank relative to the projector is not addressed in this paper. Instead, we focus on enhancing the accuracy of the robotic system in positioning the build plate with respect the resin tank.

For a relatively small robot system used in vat polymerization additive manufacturing (e.g., [3]), such as the one we are focused on, there are only a few cost-effective tools available for robot calibration. One option involves attaching a telescoping ballbar between a magnetic mount on the build plate and another on the resin tank, as described in [6]. However, this method requires extensive manual manipulation, making it impractical. Another possibility is to use a touch probe attached to the robot's tool flange to probe precision artifacts (e.g., balls) mounted on the resin tank, similar to the approach in [7]. Unfortunately, this method is not very effective, especially if the artifacts are not sufficiently spaced apart, because each measurement provides a single constraint equation. A third approach involves the use of six linear gauges and a cube artifact [8], but it allows measurement in a very small zone. A fourth, more effective approach involves the use of only three linear gauges along with precision balls. One such method, described in [9], introduces the TriCal—a cost-effective 3D probe. However, TriCal was designed to be mounted on a robot end-effector and used to probe a series of balls on a large calibration artifact (see https://youtu.be/O2vGkOy08h).

In this work, we propose a novel calibration method inspired by the approach described in [9] and tailored specifically for vat polymerization additive manufacturing, where attaching a large calibrated artifact to the resin tank is impractical. Our method uses a specialized calibration end-effector equipped with three precision balls, while the TriCal is mounted on the resin tank via a kinematic coupling and positioned in three distinct ways. This novel, patent-pending procedure is both cost-effective and semi-automated, requiring minimal human intervention.

In the following section, we describe the hardware and measurement procedure used in our experimental setup. Section 3 details the nominal direct kinematic model of the 7-DOF robotic system used in this work. In Section 4, we outline the calibration method, including the comprehensive mathematical model with parameters to be identified, the selection process for measurement joint positions, and the identification process itself. To validate our method's performance, Section 5 presents several measurement results obtained with a laser tracker. Finally, conclusions are discussed in Section 6.

2. Hardware and measurement procedure

In this section, we will describe the hardware of our experimental setup, shown in Fig. 2 during three of many self-measurements, that was used for developing and validating the calibration procedure.

In [3], a small, high-precision six-axis robot arm, the Meca500 from Mecademic, was utilized for vat polymerization additive manufacturing. To enable the production of larger parts while maintaining a compact system, the team opted to mount the robot arm on a high-accuracy linear guide, the X-LRQ300AP from Zaber Technologies. (Both the robot and the linear guide feature integrated controllers.) Our

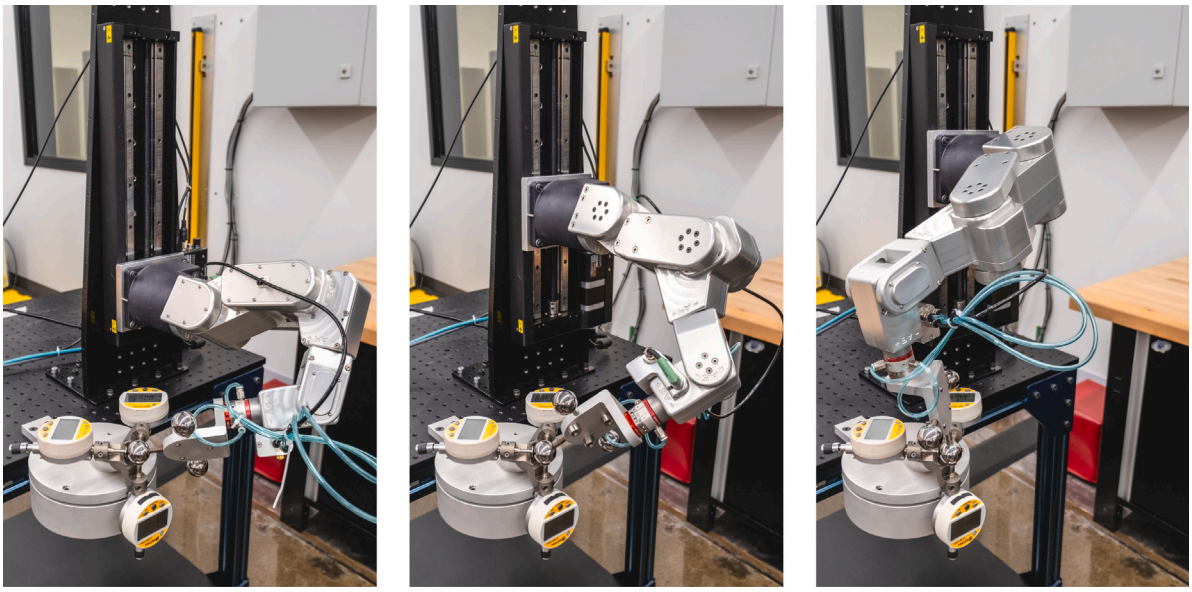

Fig. 2. The experimental setup shown during three different measurements with one calibration TCP at one calibration position.

calibration method remains essentially unchanged even if a larger six-axis robot arm is used alone. Additionally, our preliminary layout optimization indicated that the robot should be mounted as shown in Figs. 1 and 2, and a 90° build plate should be used. However, the calibration procedure is not dependent on the specific cell layout. Finally, in order to automate the calibration procedure but also the process of printing multiple parts, we used a highly-repeatable, pneumatic tool changer, SWR0010 from Kosmek.

In the vat polymerization process, the optical image projected into the resin dictates the shape of each building layer via photo-polymerization reactions. The 3D structures are created by sequentially adding these layers, making precise alignment between the projected images, resin tank, and build platform essential. This alignment can be achieved by establishing a reference frame attached to the resin tank, allowing independent alignment of the build plate and projected images.

This work focuses on accurately positioning the build plate, mounted on the robot, with respect to the resin tank. A subsequent study will develop a methodology for aligning the projected image with the resin tank. In our experimental setup, the resin tank is rigidly attached to the same base plate as the linear guide. However, in the final configuration, the tank would need to be mounted on a multi-axis positioning stage for alignment with the projected images. This would require executing the calibration procedure proposed in this paper after the tank has been aligned and secured.

2.1. 3D probe and kinematic coupling between device and resin tank

The novel measurement device comprises (1) a custom-designed 3D probe called TriCal [9] mounted on a circular *kinematic plate* and precisely positioned atop the cylindrical resin tank via (2) a Maxwell kinematic coupling. As shown in Fig. 3a, three truncated precision balls (from Bal-Tec) are equidistantly attached to the flange of the resin tank, while three pairs of parallel, high-strength alloy steel Dowel pins are embedded at the bottom of the TriCal plate. The Maxwell coupling ensures affordable, precise positioning of the TriCal plate by establishing a stable six-point contact interface, preventing over-constraint while maintaining rigidity. Three pairs of neodymium magnets are incorporated into the two components to ensure that the TriCal plate stays in constant contact with the resin tank, during measurements (Fig. 3b).

This kinematic coupling ensures not only highly repeatable positioning of the TriCal on the resin tank but also allows it to be mounted in three distinct orientations, as shown in Fig. 4. This capability is a key aspect of the novel calibration method.

TriCal was introduced in [9], where it was used to calibrate an industrial robot in a different setup than ours. As shown in Figs. 3b and 4, the device is composed of an aluminum fixture holding three linear gauges, the axes of which are (theoretically) orthogonal to each other and intersect at one point—*the origin*. A flat disk-shaped tip is mounted at the end of each of the linear gauges to ensure a plane-sphere contact with a precision ball. Therefore, TriCal can measure the 3D coordinates of the center of a properly-sized precision ball in the vicinity of TriCal's origin.

TriCal also features a trihedral socket with a neodymium magnet (Fig. 3) used to hold a precision 1.5-inch master ball, allowing for the initialization of the three gauges. When the master ball is mounted, its center defines the origin of TriCal and the gauges are set to 6.350 mm. This is done so that the gauges show a value of 0.000 mm when a 1-inch ball, mounted on the robot's end-effector, is placed at the origin of TriCal (as in Fig. 4).

Most importantly, while TriCal can measure the coordinates of a 1-inch ball positioned within 6 mm of the probe's origin, we use this measurement only to iteratively adjust the position of the ball with the robot until it is centered at TriCal's origin. In other words, *TriCal is not utilized as an absolute measurement tool, but rather to provide feedback to the robot until the robot aligns one of its 1-inch balls with TriCal's origin*. This distinction is crucial, as it eliminates the need for precise inspection of the gauge axis locations relative to each other and to the resin tank. In other words, minor deviations in orthogonality between the axes of the linear gauges and slight offsets between any two axes are acceptable.

The main innovation of our setup with respect to that of [9] is that TriCal is fixed with respect to the robot's base instead of attached on the robot's flange, and the precision balls are fixed on the end-effector of the robot. Most importantly, as already mentioned, the kinematic coupling allows us to place TriCal's origin in three precisely known locations (Fig. 4).

With the 1.5-inch master ball mounted on TriCal, we are thus able to accurately probe the three locations of TriCal's origin with respect to a base reference frame defined by the centers of the three truncated balls of the resin tank. The three positions are shown in Table 1. They

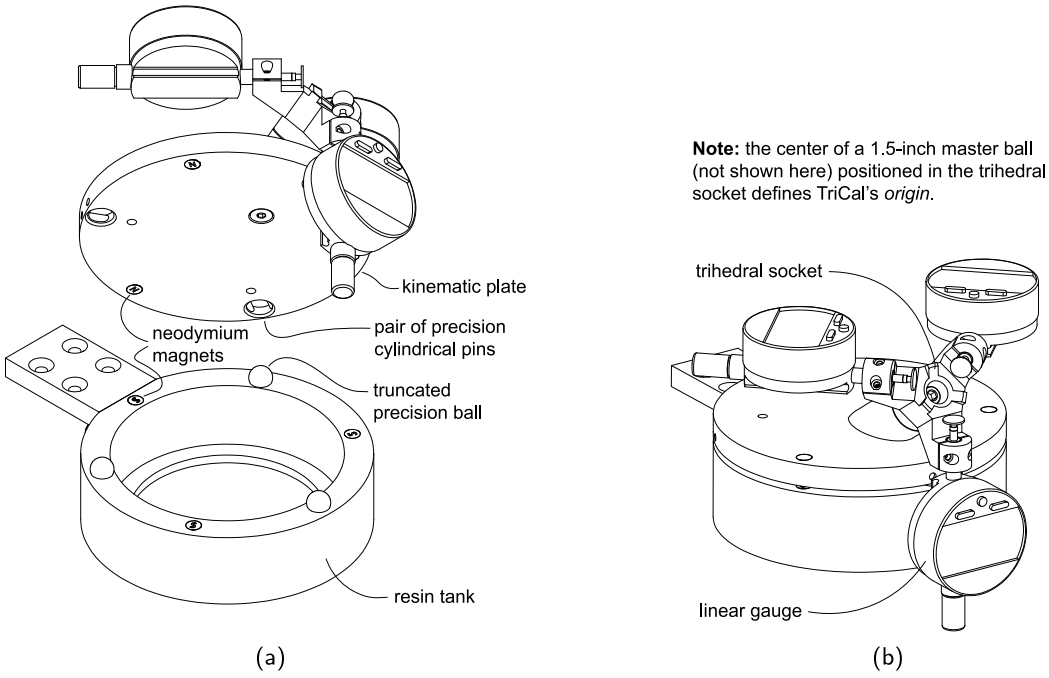

Fig. 3. The kinematic coupling between the resin tank and the kinematic plate allows TriCal to be precisely positioned in three ways.

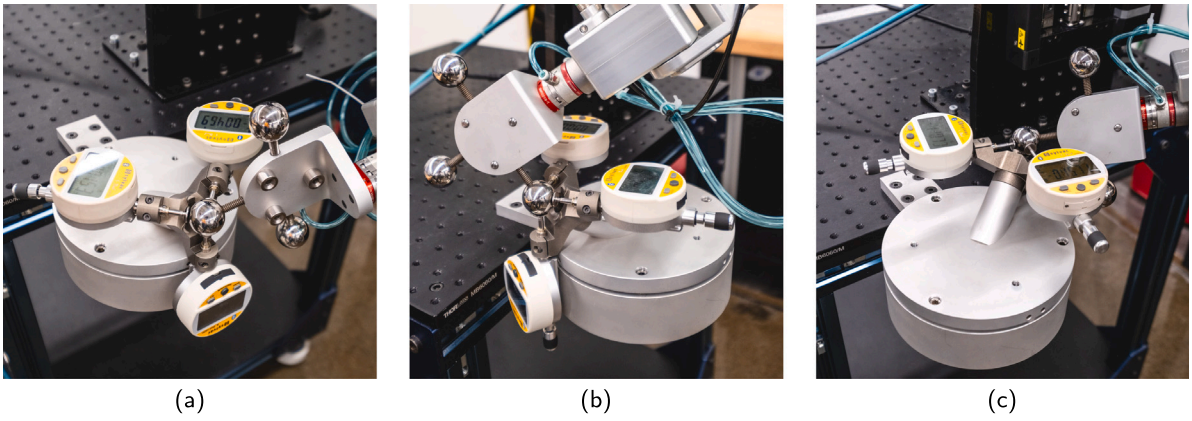

Fig. 4. The three possible ways to place the kinematic plate yield three distinct positions for TriCal's origin, which are called calibration positions.

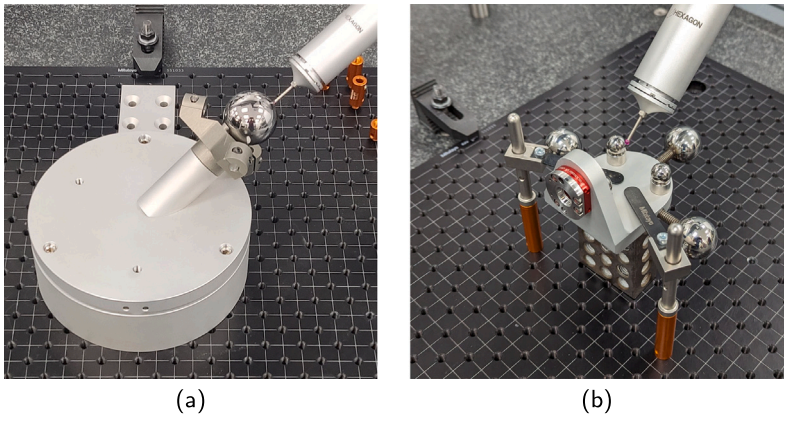

Fig. 5. Measuring on a CMM (a) TriCal's origin in each of three positions (only one shown here) with respect to the resin tank's reference frame defined by the truncated balls, and (b) the centers of the six precision balls on the calibration end-effector with respect to the tool-changer reference frame.

Table 1
The three possible positions of TriCal's origin, with respect to the world reference frame (defined by the centers of the three truncated balls on the resin tank).

Calibration position	x [mm]	y [mm]	z [mm]
1	−87.384	−0.487	47.063
2	44.144	−75.562	47.047
3	43.397	75.882	47.054

Table 2
Positions of the centers of the three 1-inch precision balls with respect to the robot tool-changer reference frame.

Calibration TCP	x [mm]	y [mm]	z [mm]
1	−56.780	30.515	67.113
2	0.214	30.189	124.590
3	56.855	30.647	66.726

were inspected on a CMM (Fig. 5a). These three locations will be called the *calibration positions* (Fig. 4). We also validated the repeatability of the kinematic coupling and its rigidity (i.e., the coupling force of the three pairs of Neodymium magnets) during measurements with TriCal, and found it to be negligible and impossible to measure by the CMM.

2.2. Calibration end-effector

The calibration end-effector is essentially shaped similarly to the build plate that will be used in the printing process. The part consists of three 1-inch precision balls, to be probed by TriCal, and three magnetic nests for 0.5-inch SMRs (spherically-mounted reflectors), for validation measurements with a laser tracker. The centers of the three 1-inch precision balls define three *calibration TCPs* (tool center points). The centers of these three balls, the three magnetic nests, and the tool changer were inspected on a CMM (Fig. 5b). The coordinates of the 1-inch balls with respect to the tool-changer reference frame are presented in Table 2.

2.3. Communication

The linear gauges used are S_Dial WORK Nano Smart digital indicators from Sylvac. They are connected via Bluetooth to a PC that runs the control, measurement and calibration algorithms, coded in Python. The Meca500 robot is connected to the PC using an Ethernet cable and controlled using Mecademic's Python API. Finally, the Zaber linear guide is also connected to the PC using an Ethernet cable and controlled using Zaber's Python API.

2.4. Measurement strategy

The idea behind our measurement strategy is to program the 7-DOF robotic system (Meca500 robot and Zaber linear guide) to automatically position each of the three calibration TCPs at the current calibration position (i.e., at the origin of TriCal in the calibration plate's current placement), with multiple joint positions. An example of three such measurement joint positions for one calibration TCP and one calibration position is shown in Fig. 2. A measurement is then taken using the linear gauges, yielding an error $\{\Delta x, \Delta y, \Delta z\}$ along the axes of a reference frame aligned with the gauges. The robot is subsequently commanded to move its calibration TCP by $\{-\Delta x, -\Delta y, -\Delta z\}$. Another measurement is taken, followed by another corrective robot movement. This *auto-centering* process is repeated until the composite position error is less than 0.005 mm. Finally, once the calibration TCP is centered at TriCal's origin, the positions of the robot joints and the linear guide are recorded.

The theory behind the optimal choice of measurement joint positions for each placement of the TriCal calibration plate will be discussed later. Once these joint positions are determined, a simulation is performed to eliminate all measurements that lead to collisions, using the Klampt Python library [10]. Next, a probabilistic optimization algorithm [11] is applied to sequence the measurements, minimizing measurement times in a manner similar to solving the traveling salesman problem. Finally, the Klamp Python library was used to find optimal, collision-free paths between each two subsequent measurements. All of these steps are performed offline and do not have to be repeated for subsequent calibrations. The computational time for these steps is about 30 min.

The complete measurement procedure is fully automated, except for the three different placements of the TriCal calibration plate. The total duration for all measurements (40) is about 25 minutes. Ideally, the robot system must be warmed up for about 30 minutes, before measurements, by performing a warm-up motion.

2.5. Measurement uncertainties

The following are the main sources of errors:

- TriCal: The maximum error of each linear gauge is 1.2 μm. The sphericity of the 1.5-inch master ball used for defining TriCal's origin and of the 1-inch balls of the calibration end-effector is 0.2 μm, while their diameter tolerance is 2.5 μm. Finally, as we already mentioned, we stop the auto-centering procedure once the composite error is less than 5 μm.
- CMM: The accuracy of the CMM we used for inspecting the calibration end-effector and the calibration positions (Hexagon Global S) is about 1.5 μm.
- Tool changer: the repeatability of Kosmek's SWR0010 tool changer is 5 μm.
- Robot arm: the position repeatability of the Meca500 is 5 μm.
- Linear guide: the repeatability of Zaber's X-LRQ300AP linear guide is 2.5 μm.

Thus, the total measurement error (less than ten micrometers) is smaller than the repeatability of the robotic system (linear guide, robot arm and tool changer), which itself is at least several times smaller than the desirable tolerance for printed parts.

3. Robot modeling

The 7-DOF robotic system, composed of the robot arm and linear guide, has been modeled using the modified Denavit–Hartenberg (MDH) convention [12]. This method defines a reference frame for each robot link based on the multiplication of a series of parametric four-dimensional homogeneous matrices, each defined by four parameters. An additional parameter was introduced between the frames of the third and fourth joints to account for the misalignment between the two parallel joint axes of the robot [13]. The eight MDH reference frames, labeled from 0 (the base frame) to 7 (the tool-changer frame), along with the world reference frame, are shown in Fig. 6.

The nominal MDH parameters are detailed in Table 3, where $d_{\mathrm{OFS},1}$ and $\theta_{\mathrm{OFS},2}$, $\theta_{\mathrm{OFS},3}, \ldots, \theta_{\mathrm{OFS},7}$ are the offsets to the active-joint variables, q_1, $q_2, \ldots, q_7$. The homogeneous transformation matrices are defined as:

$$\mathbf{H}_i^{i-1} = \mathbf{R}_x(\alpha_{i-1})\,\mathbf{T}_{xyz}(a_{i-1}, 0, 0)\,\mathbf{R}_y(\beta_{i-1})\,\mathbf{R}_z(\theta_i)\,\mathbf{T}_{xyz}(0, 0, d_i), \tag{1}$$

where α_{i-1}, a_{i-1}, d_i and θ_i, for $i = 1, 2, \ldots, 7$, are the DH parameters, and the misalignment angle β_{i-1} is used only for $i = 4$. The homogeneous matrices $\mathbf{R}_x$, $\mathbf{R}_y$ and $\mathbf{R}_z$ describe, respectively, a rotation around the axis x, y and z, and the matrix $\mathbf{T}_{xyz}$ represents a translation along the axes x, y, and z.

The pose of the world reference frame with respect to the base reference frame is defined as:

$$\mathbf{H}_{\mathrm{W}}^{0} = \mathbf{T}_{xyz}(x, y, z)\,\mathbf{R}_x(\alpha)\,\mathbf{R}_y(\beta)\,\mathbf{R}_z(\gamma). \tag{2}$$

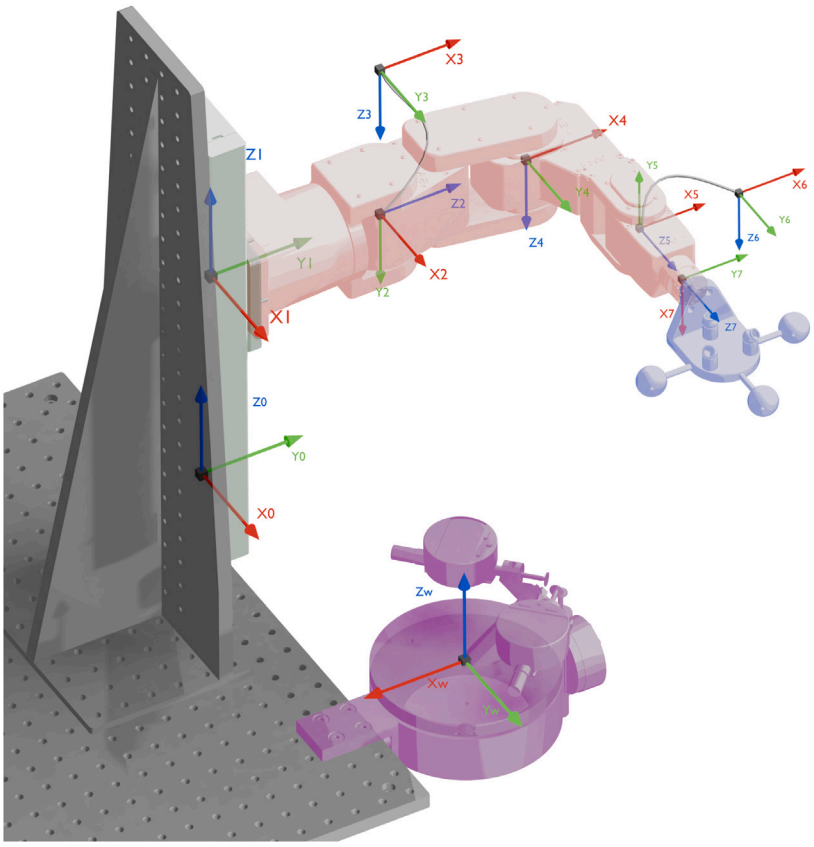

Fig. 6. MDH reference frames and world reference frame.

Table 3
Nominal Modified Denavit–Hartenberg parameters for the 7-DOF robotic system.

i	α_{i-1} [°]	a_{i-1} [mm]	d_i [mm]	θ_i [°]	$d_{\mathrm{OFS},i}$ [mm]	$\theta_{\mathrm{OFS},i}$ [°]	β_{i-1} [°]
1	0	9.65	$q_1 + d_{\mathrm{OFS},1}$	0	0	n/a	n/a
2	−90	0	135	$q_2 + \theta_{\mathrm{OFS},2}$	n/a	0	n/a
3	−90	0	0	$q_3 + \theta_{\mathrm{OFS},3}$	n/a	−90	n/a
4	0	135	0	$q_4 + \theta_{\mathrm{OFS},4}$	n/a	0	0
5	−90	38	120	$q_5 + \theta_{\mathrm{OFS},5}$	n/a	0	n/a
6	90	0	0	$q_6 + \theta_{\mathrm{OFS},6}$	n/a	0	n/a
7	−90	0	70	$q_7 + \theta_{\mathrm{OFS},7}$	n/a	−180	n/a

The complete system's geometrical model is made up of the MDH robot arm model, the pose of the world reference frame (at the resin tank) with respect to the base frame (frame 0), and the positions of the calibration TCPs with respect to the tool-changer frame. The position of the calibration TCPs with respect to the world reference frame (resin tank) is defined as:

$$\mathbf{H}^{\mathrm{W}}_{\mathrm{T}_i} = \mathbf{H}^{\mathrm{W}}_{0}\,\mathbf{H}^{0}_{1}\,\mathbf{H}^{1}_{2}\,\mathbf{H}^{2}_{3}\,\mathbf{H}^{3}_{4}\,\mathbf{H}^{4}_{5}\,\mathbf{H}^{5}_{6}\,\mathbf{H}^{6}_{7}\,\mathbf{H}^{7}_{\mathrm{T}_i} = \begin{bmatrix} \cdots & \cdots & \cdots & p_{i,x} \\ \cdots & \cdots & \cdots & p_{i,y} \\ \cdots & \cdots & \cdots & p_{i,z} \\ 0 & 0 & 0 & 1 \end{bmatrix}. \tag{3}$$

In addition, a stiffness parameter has been added to account for the effect of gravity on the Meca500 links. The mass of the robot links and the calibration tool is not negligible and exerts a torque on each of the robot's joints that is a function of the robot joint position. This parameter, c_i, is obtained by linearization of the effect of the torque on the angle of the ith joint [12]. In other words, we model each joint as a rotary spring, with c_i being the spring compliance. In the nominal model, $c_i = 0$, for all six joints.

The procedure for calculating the torque on each joint of the robot has been detailed in [9,12]. It consists of two iterating equations that must be computed. The first of these is an outward iteration, which proceeds from link 2 to link 7 (from the robot base to the tool changer) and is used to find the rotation of each link in space. The second is an inward iteration proceeding from link 7 to link 2, which is used to compute the effect of the mass of all the following links, held by the ith joint, and result in six equations of this form:

$$\tau_i = f_i(\theta_2, \cdots, \theta_7), \tag{4}$$

where θ_j are the robot joint angles, and τ_i is the torque applied by gravity on the ith joint.

When modeling the errors in all of the nominal parameters (the pose of the world reference frame with respect to the base reference frame and the parameters in Table 3), it can be observed that some of these errors are redundant. These can be identified using a matrix rank analysis on the observability Jacobian $\boldsymbol{\Gamma}_0$ described in Eq. (12). The selected, identifiable parameters are shown in Tables 4 and 5. Each identifiable parameter is expressed as its nominal value plus an error component prefixed by δ, as in $\alpha_1 + \delta\alpha_1$. Note that we do not need to identify the coordinates of the calibration TCPs with respect to the tool-changer frame, because these were inspected on a CMM. Thus, our calibration method must identify a total of 34 errors.

Table 4
Base reference frame pose with respect to (w.r.t.) world reference frame and positions of TCP i ($i = 1, 2, 3$) w.r.t. to tool-changer frame.

	x [mm]	y [mm]	z [mm]	α [°]	β [°]	γ [°]
Base frame w.r.t world frame	$x_0^{\mathrm{W}} + \delta x_0^{\mathrm{W}}$	$y_0^{W} + \delta y_0^{\mathrm{W}}$	$z_0^{\mathrm{W}} + \delta z_0^{\mathrm{W}}$	$\alpha_0^{\mathrm{W}} + \delta\alpha_0^{\mathrm{W}}$	$\beta_0^{\mathrm{W}} + \delta\beta_0^{\mathrm{W}}$	$\gamma_0^{\mathrm{W}} + \delta\gamma_0^{\mathrm{W}}$
TCPs w.r.t. tool-changer frame	$x_{\mathrm{T}_i}^7$	$y_{\mathrm{T}_i}^7$	$z_{\mathrm{T}_i}^7$	n/a	n/a	n/a

Table 5
Kinematic parameters and revolute joint stiffness parameters.

i	α_{i-1} [°]	a_{i-1} [mm]	d_i [mm]	θ_i [°]	β_{i-1} [°]
1	α_0	a_0	q_1	θ_1	n/a
2	$\alpha_1 + \delta\alpha_1$	a_1	d_2	$q_2 + \theta_{\mathrm{OFS},2} + \delta\theta_{\mathrm{OFS},2} + (c_2 + \delta c_2)\tau_2$	n/a
3	$\alpha_2 + \delta\alpha_2$	$a_2 + \delta a_2$	d_3	$q_3 + \theta_{\mathrm{OFS},3} + \delta\theta_{\mathrm{OFS},3} + (c_3 + \delta c_3)\tau_3$	n/a
4	$\alpha_3 + \delta\alpha_3$	$a_3 + \delta a_3$	$d_4 + \delta d_4$	$q_4 + \theta_{\mathrm{OFS},4} + \delta\theta_{\mathrm{OFS},4} + (c_4 + \delta c_4)\tau_4$	$\beta_3 + \delta\beta_3$
5	$\alpha_4 + \delta\alpha_4$	$a_4 + \delta a_4$	$d_5 + \delta d_5$	$q_5 + \theta_{\mathrm{OFS},5} + \delta\theta_{\mathrm{OFS},5} + (c_5 + \delta c_5)\tau_5$	n/a
6	$\alpha_5 + \delta\alpha_5$	$a_5 + \delta a_5$	$d_6 + \delta d_6$	$q_6 + \theta_{\mathrm{OFS},6} + \delta\theta_{\mathrm{OFS},6} + (c_6 + \delta c_6)\tau_6$	n/a
7	$\alpha_6 + \delta\alpha_6$	$a_6 + \delta a_6$	$d_7 + \delta d_7$	$q_7 + \theta_{\mathrm{OFS},7} + \delta\theta_{\mathrm{OFS},7} + (c_7 + \delta c_7)\tau_7$	n/a

Table 6
Detmax algorithm for observability analysis.

1	Randomly select an initial set of n candidates from the initial set of N candidates (master set).
2	From the remaining $(N - n)$ candidates, evaluate each one's contribution to the observability index. Add the candidate with the highest contribution to the current set, forming a new set of $n + 1$ candidates.
3	From the new set of $n + 1$ candidates, remove the one with the least contribution to the observability index, bringing the set back to n candidates.
4	Repeat steps 2 and 3 until the candidate added in step 2 is the same one removed in step 3.

4. Calibration method

Once a new, comprehensive mathematical model is established, we will need measurement data to identify the parameters of this new model.

4.1. Obtaining measurable robot joint positions

First, we generated a set of N random measurement joint positions $\{q_1, q_2, q_3, q_4, q_5, q_6, q_7\}$. This is done by calculating the inverse kinematics of the 7-DOF robot system for 500 random orientations of the robot's end-effector, for each of the three calibration TCPs at each of the three calibration positions, resulting in an initial set of 4,500 end-effector measurement poses.

Since the robotic system is redundant, each end-effector pose has infinitely many possible inverse kinematics solutions, i.e., infinitely many joint positions. To manage this, we discretized the range of the linear guide into ten positions. For each position of the linear guide, the 6-DOF robot arm has up to eight inverse kinematics solutions. Therefore, for each end-effector pose, we obtained up to 80 joint positions.

From the initial set of up to 80 times 4,500 candidates, we eliminated the joint positions that resulted in mechanical interferences, leaving a total of $N = 3,284$ measurable joint positions.

4.2. Selecting the optimal measurable joint positions

An observability analysis was performed to reduce the number of measured joint positions, thereby minimizing calibration time while preserving the accuracy of parameter identification. The algorithm, previously described in the literature [14,15], selects a subset of n measurable joint positions from the master set of N positions, where $n \ll N$.

The algorithm used, called Detmax [16], iteratively maximizes a cost function that characterizes the quality of the n selected measurements. This approach avoids the need to evaluate all possible configurations of n positions out of N. The cost function, known as the observability index [14,17], is optimized by the Detmax algorithm, which is outlined in Table 6.

The optimal value of n was determined by calculating the number of equations required to describe the 34 calibrated parameters of the robot model presented in Section 3. Since each measured position provides three equations (x, y, z), a minimum of 13 measurements is required. However, to reduce the impact of measurement noise while maintaining a fast calibration process, we selected $n = 40$ measurements. By using the Detmax algorithm, we avoided having to compute $\binom{4000}{40} \approx 10^{96}$ observability indices.

Note that removing one or two of the three calibration positions leads to a drastic decrease of the observability index and thus the quality of the calibration process. In fact, the value of the O1 observability index [15] varies from 0.5 with one position, to 4.6 for two positions, and 15.2 with three positions. This highlights the importance of having at least three calibration positions. Indeed, with fewer than three positions, it is impossible to identify all six pose parameters of the world reference frame. Furthermore, although the calibration positions are in close proximity (each pair is only about 151 mm apart), each position enables the robot's end-effector to adopt a distinct set of orientations (recall Fig. 4), resulting in three sets of significantly different joint positions.

4.3. Measurement process

The measurement procedure involves moving the robot to each of the 40 selected joint positions and automatically centering the TCP position until the composite error measured by TriCal is less than 0.005 mm. Then, the robot's joint values are recorded and saved. (During the auto-centering procedure, only the robot is moved, and the linear guide is kept stationary, so the value of d_1 does not change.) For each of the 40 measured positions, the Cartesian error is calculated by comparing the position from the direct kinematics of the initial joint position with that of the joint position after the TCP auto-centering.

4.4. Identification of the 34 error parameters

These 40 Cartesian error values are then saved in the vector $\mathbf{x}_{\mathrm{meas}}$ of size 120:

$$\mathbf{x}_{\mathrm{meas}} = \begin{pmatrix} d_{x1} & d_{y1} & d_{z1} & \cdots & d_{x40} & d_{y40} & d_{z40} \end{pmatrix}. \tag{5}$$

The seven active-joint variables are represented by the following vector:

$$\mathbf{q} = \begin{pmatrix} q_1 & \cdots & q_7 \end{pmatrix}. \tag{6}$$

The 34 identifiable parameters listed in Tables 4 and 5 have been combined into a single vector:

$$\boldsymbol{\rho} = \begin{pmatrix} \boldsymbol{\alpha} & \mathbf{a} & \mathbf{d} & \boldsymbol{\theta}_{\text{OFS}} & \beta_3 & \mathbf{c} & \chi_0 \end{pmatrix}, \tag{7}$$

where

$$\begin{aligned}
\boldsymbol{\alpha} &= \begin{pmatrix} \alpha_1 & \cdots & \alpha_6 \end{pmatrix}, \\
\mathbf{a} &= \begin{pmatrix} a_2 & \cdots & a_6 \end{pmatrix}, \\
\mathbf{d} &= \begin{pmatrix} d_4 & \cdots & d_7 \end{pmatrix}, \\
\boldsymbol{\theta}_{\text{OFS}} &= \begin{pmatrix} \theta_{\text{OFS},2} & \cdots & \theta_{\text{OFS},7} \end{pmatrix}, \\
\mathbf{c} &= \begin{pmatrix} c_2 & \cdots & c_7 \end{pmatrix}, \\
\chi_0 &= \begin{pmatrix} x_0^{\text{W}} & y_0^{\text{W}} & z_0^{\text{W}} & \alpha_0^{\text{W}} & \beta_0^{\text{W}} & \gamma_0^{\text{W}} \end{pmatrix}.
\end{aligned}$$

Then, Eq. (3) has been computed using the variables of Tables and Tables 4 and 5 with all $\delta = 0$. The three elements of the parametric position of the calibration TCP (p_x, p_y, p_z) of this matrix have been partially derived with respect to each of the calibrated parameters $\boldsymbol{\rho}$, giving us the following matrix:

$$\mathbf{J} = \begin{bmatrix} \frac{\partial p_x}{\partial \rho_1} & \frac{\partial p_x}{\partial \rho_2} & \cdots & \frac{\partial p_x}{\partial \rho_{34}} \\ \frac{\partial p_y}{\partial \rho_1} & \frac{\partial p_y}{\partial \rho_2} & \cdots & \frac{\partial p_y}{\partial \rho_{34}} \\ \frac{\partial p_z}{\partial \rho_1} & \frac{\partial p_z}{\partial \rho_2} & \cdots & \frac{\partial p_z}{\partial \rho_{34}} \end{bmatrix}. \tag{8}$$

The resulting matrix is called the observability Jacobian, and is essentially quantifying the impact of each of the 34 parameters on the position of the tool with respect to the resin tank. This matrix is function of the robot joint $\mathbf{q}$ and the calibrated values $\boldsymbol{\rho}$. The torque value on each of the robot's revolute joints, $\boldsymbol{\tau} = (\tau_1 \cdots \tau_6)$, has been expressed as a function of $\mathbf{q}$ in Eq. (4) and is therefore not mentioned as a independent variable nor derived with respect to $\mathbf{q}$, due to computational time.

The linearized expression of a small position deviation $\Delta\mathbf{P} = (\Delta p_x, \Delta p_y, \Delta p_z)$ as a function of a small parameter deviation $\Delta\boldsymbol{\rho}$ is given by :

$$\Delta\mathbf{P} = \mathbf{J}\Delta\boldsymbol{\rho}. \tag{9}$$

To obtain a reverse expression of the impact of the tool position on the 34 identifiable parameters, the Moore–Penrose inverse has been used. In our case, the following equation gives the small parameter deviation $\Delta\boldsymbol{\rho}$ as a function of a small position deviation $\Delta\mathbf{P}$:

$$\Delta\boldsymbol{\rho} = \left(\mathbf{J}^T\mathbf{J}\right)^{-1}\mathbf{J}^T\Delta\mathbf{P} = \mathbf{J}^+\Delta\mathbf{P}. \tag{10}$$

Next, the pseudo inverse Jacobian, $\mathbf{J}^+$, can be evaluated with the nominal parameter values $\boldsymbol{\rho}_0$, creating a function of the joint position, $\mathbf{J}_0^+(\mathbf{q})$, of size 34×3:

$$\mathbf{J}_0^+(\mathbf{q}) = \mathbf{J}^+(\mathbf{q}, \boldsymbol{\rho}_0). \tag{11}$$

Using the values of the joints used for the 40 measures $\mathbf{q}_{meas,k}$, k ranging from 1 to 40, we can build a correction matrix of size 34×120:

$$\boldsymbol{\Gamma}_\mathbf{0} = \begin{pmatrix} \mathbf{J}_0^+(\mathbf{q}_{\text{meas},1}) & \cdots & \mathbf{J}_0^+(\mathbf{q}_{\text{meas},40}) \end{pmatrix}. \tag{12}$$

The values of the small parameter deviation can now be evaluated,

$$\Delta\boldsymbol{\rho}_0 = \boldsymbol{\Gamma}_\mathbf{0}\mathbf{x}_{\text{meas},0}, \tag{13}$$

and added to the calibrated parameter values,

$$\boldsymbol{\rho}_1 = \boldsymbol{\rho}_0 + \Delta\boldsymbol{\rho}_0. \tag{14}$$

Then, the measured Cartesian errors $\mathbf{x}_{\text{meas}}$ described in Eq. (5) are re-evaluated using the new MDH and stiffness parameter values $\boldsymbol{\rho}_1$, giving us the vector $\mathbf{x}_{\text{meas},1}$. Eq. (11) is repeated to build $\mathbf{J}_1^+(\mathbf{q})$ using the values of $\boldsymbol{\rho}_1$. This allows for the calculation of $\boldsymbol{\Gamma}_1$, $\Delta\boldsymbol{\rho}_1$ and $\boldsymbol{\rho}_2$.

The process is described in Table 7. Ideally, ϵ_{i+1} will converge to zero, meaning that the calibrated model is obtaining exactly the same Cartesian errors at the same joint values measured during the procedure described in Section 4.3. However, the mean of errors will always converge to a non-zero value, due to approximations made during the robot modeling.

5. Validation using a laser tracker

To evaluate the performance of the proposed calibration method, we used a brand-new FARO Vantage E laser tracker, as shown in Fig. 7b. The distance accuracy according to its recent calibration is 16 µm (in our measurement volume). We placed three brand-new 0.5-inch SMRs in the magnetic nests of the calibration end-effector, as shown in Fig. 7b. Recall that the centers of these nests were inspected on a CMM with respect to the same tool-changer reference frame that was used in the proposed calibration method (Fig. 5a). The vertex (the intersection of the three mirrors) in each SMR is centered within ±13 µm of the center of the sphere. Thus, to reduce measurement errors, the SMRs were not reoriented inside their nests during measurements. However, this means that we can have as much as about 20 µm of measurement errors.

Finally, we placed a 1-inch SMR in the TriCal trihedral nest and inspected the three calibration positions using the laser tracker (Fig. 7c). Consequently, the measurements with the laser tracker were reported in the same world reference frame as in the proposed calibration procedure. However, as with the small SMRs, we have as much as 20 µm of measurement errors in measuring the world reference frame.

We then simulated a large number of random joint positions, retaining only those where at least one of the three 0.5-inch SMRs was visible to the laser tracker and where no mechanical interferences occurred. During the actual measurements, some of these joint positions were not measurable due to SMR visibility issues. As a result, we measured the positions of one or another of the three SMRs in a total of 573 joint positions, corresponding to 573 end-effector poses distributed throughout the entire accessible workspace of the 7-DOF robotic system.

Fig. 8 shows the histogram of the measured errors before calibration (i.e., using the nominal values for all parameters) and after calibration (i.e., using the values identified by the proposed calibration method). There is a significant improvement in the system's positioning performance, with the mean position error reduced from 1.272 mm to 0.271 mm.

On one hand, the 7-DOF robotic system is not intended to print parts throughout its entire accessible workspace, and accuracy will be higher near the resin tank. Recall that the larger workspace is essential not only for printing larger parts but also for automating subsequent processes and stacking multiple printed parts (Fig. 1). On the other hand, a limitation of robot-held part printing is that as printing progresses, the area requiring accuracy (in our case, the bottom of the resin tank) moves farther from the robot's end-effector (the build plate). This increasing distance can amplify small orientation errors in the build plate throughout the printing process (lever effect).

We therefore simulated a potential six-dimensional printing path and measured the position of the three SMRs in each of the 300 slices along the path. This allows us to compute the pose (position and orientation) of the end-effector, that we can then transform toward the end of the theoretical printed part (where the material is being added). The path and the position errors along the path (at the resin tank bottom) are shown in Figs. 9 and 10. The mean of the positioning errors after calibration is now 0.220 mm, which is much better that the mean positioning error before calibration (1.192 mm).

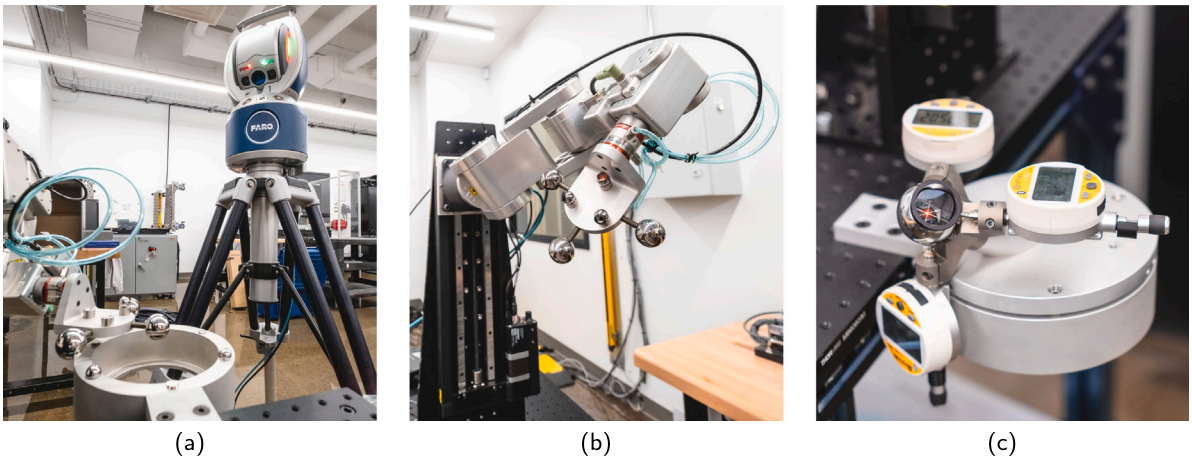

Fig. 7. Using a FARO Vantage laser tracker to validate the positioning accuracy of the complete robot system after calibration.

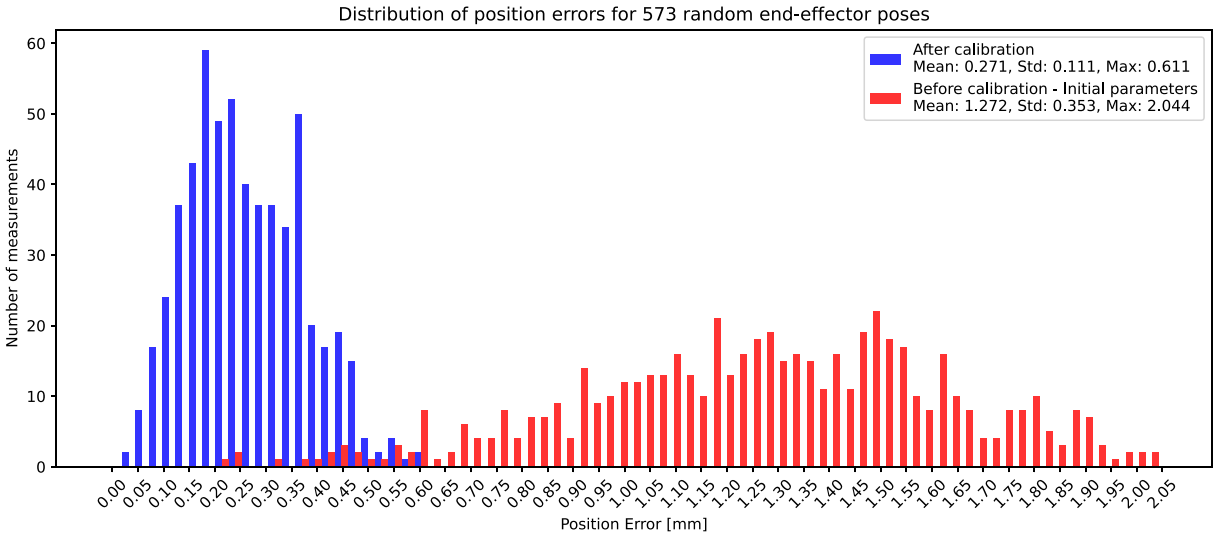

Fig. 8. Frequency of position errors before and after calibration for random joint positions (i.e., random end-effector poses) as measured by a laser tracker.

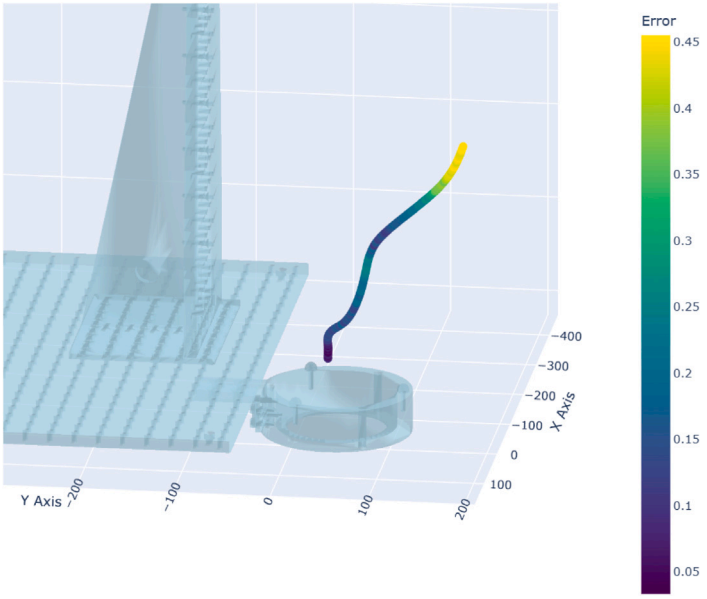

Fig. 9. 3D plot of positioning errors at resin tank for a sample printing path (all units are mm).

Table 7
Calibrated parameter evaluation algorithm for 40 measurements.

1	Evaluate the error $\mathbf{x}_{\text{meas},i}$ using forward kinematic with the parameters $\boldsymbol{\rho}_i$
2	Use the parameters $\boldsymbol{\rho}_i$ to compute the observability matrix $\mathbf{J}_i^+(\mathbf{q})$
3	Construct the matrix $\boldsymbol{\Gamma}_i$ by concatenating $\mathbf{J}_i^+(\mathbf{q})$ on the measured robot joint targets $\mathbf{q}_{\text{meas},k}$ $k \in [1,40]$
4	Compute the correction for calibrated parameters $\Delta\boldsymbol{\rho}_i = \boldsymbol{\Gamma}_i \mathbf{x}_{\text{meas},i}$
5	Find the new calibrated parameter values $\boldsymbol{\rho}_{i+1} = \boldsymbol{\rho}_i + \Delta\boldsymbol{\rho}_i$
6	Evaluate the error $\mathbf{x}_{\text{meas},i+1}$ using forward kinematic with the parameters $\boldsymbol{\rho}_{i+1}$
7	Calculate the mean of the 40 Cartesian errors $\epsilon_{i+1} = \text{mean}\left(\sqrt{d_{x,k}^2 + d_{y,k}^2 + d_{z,k}^2}, k \in [1,40]\right)$, where $d_{x,k}$, $d_{y,k}$, $d_{z,k}$, are the elements of $\mathbf{x}_{\text{meas},i+1}$
8	Repeat steps 1 to 6 until $\lvert\epsilon_{i+1} - \epsilon_{i+2}\rvert << 0$

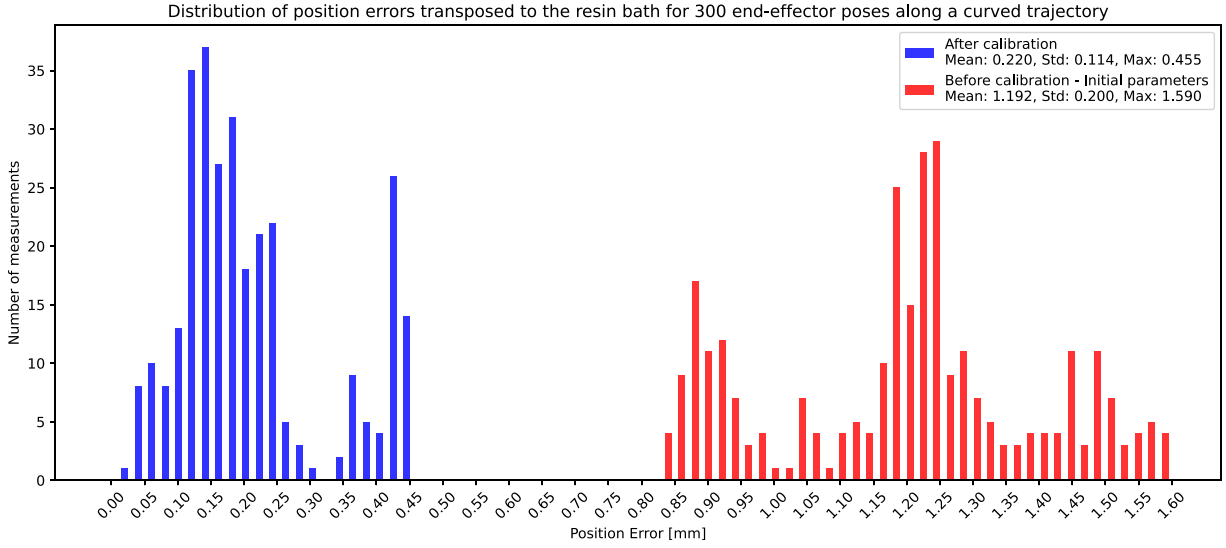

Fig. 10. Graph of positioning errors for a sample printing path.

6. Conclusions

We proposed an innovative and cost-effective calibration method applicable to any robot-held part printing system. This method builds upon an established approach and 3D probe to automatically align points from a specialized calibration end-effector with points on the base. The key novelty lies in placing the probe on the base and employing a kinematic coupling to precisely position the probe in three distinct ways.

Measurements using a laser tracker demonstrated that this method could improve 3D printing accuracy by nearly fivefold. The calibration and validation phases are illustrated in the following video: https://youtu.be/NO9TVD-Zv2k.

The proposed method was specifically developed for very small, ultra-precise robot arms whose end-effectors cannot carry a 3D probe and for applications requiring high accuracy within a relatively small volume. It could also be beneficial for slightly larger robot arms, though the kinematic coupling would likely need to be modified to allow more than three probe locations, which would slightly increase the overall cost.

Future research will focus on developing redundancy resolution algorithms that prioritize displacement of the linear guide, due to its superior accuracy within the system. In parallel, the complete additive manufacturing setup will be assembled, along with a method and system for aligning the resin tank with the projected images. Successful implementation of this step will enable 3D printing of large structures along a curvilinear printing path, while maintaining dimensional accuracy and surface smoothness. Additionally, the use of a highly repeatable tool changer will provide the flexibility to multi-task the robot for post-processing steps, thereby improving overall throughput.

CRediT authorship contribution statement

Evan Rolland: Writing – original draft, Visualization, Validation, Software, Resources, Investigation, Conceptualization. **Yasser Krim:** Resources, Investigation, Formal analysis, Conceptualization. **Ahmed Joubair:** Writing – review & editing, Supervision. **Ilian A. Bonev:** Writing – review & editing, Supervision, Resources, Project administration, Methodology, Funding acquisition, Conceptualization. **Evan Jones:** Investigation, Conceptualization. **Pengpeng Zhang:** Investigation, Conceptualization. **Cheng Sun:** Writing – review & editing, Supervision, Conceptualization. **Nanzhu Zhao:** Writing – review & editing, Supervision, Funding acquisition, Conceptualization.

Declaration of competing interest

The authors declare the following financial interests/personal relationships which may be considered as potential competing interests: Ilian Bonev reports financial support was provided by Mitacs Canada. Ilian Bonev reports financial support was provided by Nissan North America Inc. Ilian Bonev reports a relationship with Mecademic that includes: equity or stocks. If there are other authors, they declare that they have no known competing financial interests or personal relationships that could have appeared to influence the work reported in this paper.

Acknowledgments

The authors would like to thank Nissan North America Inc. and Mitacs for funding this research work.

Data availability

No data was used for the research described in the article.

References

[1] P.M. Bhatt, R.K. Malhan, A.V. Shembekar, Y.J. Yoon, S.K. Gupta, Expanding capabilities of additive manufacturing through use of robotics technologies: A survey, Addit. Manuf. 31 (2020) 100933, http://dx.doi.org/10.1016/j.addma.2019.100933.

[2] A. De Marzi, M. Vibrante, M. Bottin, G. Franchin, Development of robot assisted hybrid additive manufacturing technology for the freeform fabrication of lattice structures, Addit. Manuf. 66 (2023) 103456, http://dx.doi.org/10.1016/j.addma.2023.103456.

[3] J. Huang, H.O.T. Ware, R. Hai, G. Shao, C. Sun, Conformal geometry and multimaterial additive manufacturing through freeform transformation of building layers, Adv. Mater. 33 (11) (2021) 2005672.

[4] A. Nubiola, I.A. Bonev, Absolute calibration of an ABB IRB 1600 robot using a laser tracker, Robot. Comput.-Integr. Manuf. 29 (1) (2013) 236–245, http://dx.doi.org/10.1016/j.rcim.2012.06.004.

[5] Mecademic, Calibration services, URL https://mecademic.com/services/calibration/.

[6] A. Nubiola, I.A. Bonev, Absolute robot calibration with a single telescoping ballbar, Precis. Eng. 38 (3) (2014) 472–480, http://dx.doi.org/10.1016/j.precisioneng.2014.01.001.

[7] A. Joubair, I.A. Bonev, Kinematic calibration of a six-axis serial robot using distance and sphere constraints, Int. J. Adv. Manuf. Technol. 77 (1) (2015) 515–523, http://dx.doi.org/10.1007/s00170-014-6448-5.

[8] Y. Liu, Z. Zhuang, Y. Li, Closed-loop kinematic calibration of robots using a six-point measuring device, IEEE Trans. Instrum. Meas. 71 (2022) 1–12, http://dx.doi.org/10.1109/TIM.2022.3191707.

[9] C. Icli, O. Stepanenko, I. Bonev, New method and portable measurement device for the calibration of industrial robots, Sensors 20 (20) (2020) http://dx.doi.org/10.3390/s20205919.

[10] Kris Hauser and contributors, Klampt: Kris' locomotion and manipulation planning toolkit, 2024, GitHub repository, https://github.com/krishauser/Klampt.

[11] S.E.H. Shmul, fast-tsp: A fast solver for the traveling salesman problem (TSP), 2024, GitHub repository, https://github.com/shmulvad/fast-tsp.

[12] J.J. Craig, Introduction to Robotics: Mechanics and Control, fourth ed., Pearson, Upper Saddle River, NJ, USA, 2018.

[13] S. Hayati, K. Tso, G. Roston, Robot geometry calibration, in: Proceedings. 1988 IEEE International Conference on Robotics and Automation, 1988, pp. 947–951 vol.2, http://dx.doi.org/10.1109/ROBOT.1988.12181.

[14] J.-H. Borm, C.-H. Meng, Determination of optimal measurement configurations for robot calibration based on observability measure, Int. J. Robot. Res. 10 (1) (1991) 51–63, http://dx.doi.org/10.1177/027836499101000106.

[15] A. Joubair, I.A. Bonev, Comparison of the efficiency of five observability indices for robot calibration, Mech. Mach. Theory 70 (2013) 254–265, http://dx.doi.org/10.1016/j.mechmachtheory.2013.07.015.

[16] T.J. Mitchell, An algorithm for the construction of "D-Optimal" experimental designs, Technometrics 42 (1) (2000) 48–54, http://dx.doi.org/10.1080/00401706.2000.10485978.

[17] Y. Sun, J.M. Hollerbach, Observability index selection for robot calibration, in: 2008 IEEE International Conference on Robotics and Automation, 2008, pp. 831–836, http://dx.doi.org/10.1109/ROBOT.2008.4543308.